FIG: FLOW WITH INTERPOLANT GUIDANCE FOR LINEAR INVERSE PROBLEMS

Anonymous authors
Paper under double-blind review

ABSTRACT

Diffusion and flow matching models have been recently used to solve various linear inverse problems such as image restoration. Using a pre-trained diffusion or flow-matching model as a prior, most existing methods modify the reverse-time sampling process by incorporating the likelihood information from the measurement. However, they struggle in challenging scenarios, e.g., in case of high measurement noise or severe ill-posedness. In this paper, we propose Flow with Interpolant Guidance (FIG), an algorithm where reverse-time sampling is efficiently guided with measurement interpolants through theoretically justified schemes. Experimentally, we demonstrate that FIG efficiently produces highly competitive results on a variety of linear image reconstruction tasks on natural image datasets. We improve upon state-of-the-art baseline algorithms, especially for challenging tasks. The code will be released.

1 INTRODUCTION

Linear inverse problems have long been an active field of research in applied mathematics, statistics, and signal processing. In particular, linear inverse problems such as image restoration have many real-world applications. A typical mathematical model for linear inverse problems reads as follows:

$$\boldsymbol{y} = \boldsymbol{A}\boldsymbol{x}^* + \boldsymbol{n}, \tag{1}$$

where $\boldsymbol{y} \in \mathbb{R}^n$ is the observed measurement, $\boldsymbol{x}^* \in \mathbb{R}^d$ denotes the underlying true signal, $\boldsymbol{A} \in \mathbb{R}^{n \times d}$ is a linear forward measurement operator, and $\boldsymbol{n} \in \mathbb{R}^n$ is the measurement noise independent of signal $\boldsymbol{x}^*$. The goal of solving a linear inverse problem is to retrieve the underlying signal $\boldsymbol{x}^*$ given the observed measurement. In real-world scenarios, the problem is often ill-posed, i.e., the underlying signal is high dimensional compared to the number of observations. Formally, $n \ll d$, in which case the solution to the inverse problem is not unique. From a Bayesian perspective, the prior is given by a data representation of the underlying true signal, and the inverse problem can be solved by calculating the posterior using the measurement likelihood (Idier, 2013).

Recent developments in continuous normalizing flows have shown tremendous success in sampling from underlying complex high-dimensional distributions (Chen et al., 2018). Particularly, flow matching models (Lipman et al., 2023; Liu et al., 2023b; Albergo & Vanden-Eijnden, 2023; Albergo et al., 2023; Ma et al., 2024) together with diffusion models (Song et al., 2021b; Ho et al., 2020; Song et al., 2021a; Rombach et al., 2022), emerge as powerful tools for image synthesis (Dhariwal & Nichol, 2021). The idea behind both models is to simulate a process that gradually perturbs data until it becomes random noise. Moving from data to noise, usually referred to as forward process, can be represented by either a stochastic differential equation (SDE) or an ordinary differential equation (ODE) (Song et al., 2021b; Lipman et al., 2023). A score or velocity network is trained using the forward process to "memorize" the dynamics. Then one can generate new data from noise by time-reversing the memorized dynamics, which is usually referred to as the reverse process. In practice, velocity and score networks can be accurately learned so that the generation quality of flow matching and diffusion models is high especially for image data.

Due to the aforementioned advantages, flow matching and diffusion models have frequently been adopted to solve inverse problems for imaging data (Jalal et al., 2021). Specifically, for linear inverse problems, recent works use pre-trained flow matching or diffusion models as a prior, and guide it towards the posterior by incorporating the measurement likelihood. Though existing methods achieve highly competitive results, most of them are either slow in inference, or struggle in challenging tasks.

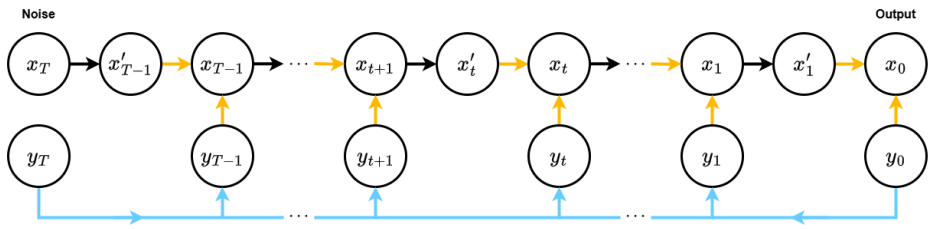

Figure 1: Overview of our FIG algorithm during the conditional sampling process. Black arrows (→) denote the unconditional update. Orange arrows (→) represent K times conditional updates with unconditional sample $\boldsymbol{x}'_t$ and measurement interpolant $\boldsymbol{y}_t$ at each timestep t. Blue arrows (→) indicate the measurement interpolation.

In this work, we propose a simple yet effective algorithm for linear inverse problems named 'Flow with Interpolant Guidance' (FIG). We summarize its mechanism in Fig. 1. In FIG, the measurement $\boldsymbol{y}$ is interpolated parallel to the forward process to obtain measurement interpolants $\{\boldsymbol{y}_t\}_{t\in[0,T]}$. Then the likelihood of $\boldsymbol{y}_t$ is used to perturb the reverse process. Our key contributions are summarized as follows:

- We propose a novel algorithm FIG that applies to all linear forward measurement operators and pre-trained models irrespective of complexity.
- We show that the updating scheme of FIG is theoretically justified.
- We implement FIG using both flow matching and diffusion models to solve various linear image reconstruction tasks, including challenging scenarios such as high measurement noise and severe ill-posedness. Results demonstrate that FIG achieves state-of-the-art performance with competitive runtime and memory consumption.

2 Background and Related Works

2.1 Flow matching and Diffusion models

Though various formulations were proposed, flow matching generally defines a continuous-time stochastic process $\{\boldsymbol{x}_t\}_{t\in[0,T]}$ for some $T \in (0, \infty]$, where $\boldsymbol{x}_0 = \boldsymbol{x}^*$ refers to the data distribution that one aims to draw samples from, and $\boldsymbol{x}_T = \boldsymbol{\varepsilon}_x$ is a noise variable that is easy to obtain. The marginal distribution of $\boldsymbol{x}_t$ for $t \in (0, T)$ is defined as an interpolant between the two boundaries, i.e.,

$$\boldsymbol{x}_t = \alpha_t \boldsymbol{x}_0 + \sigma_t \boldsymbol{x}_T, \tag{2}$$

where $\{\alpha_t\}_{t\in[0,T]}$ and $\{\sigma_t\}_{t\in[0,T]}$ are two smooth interpolation coefficients such that $\alpha_0 = \sigma_T = 1$ and $\alpha_T = \sigma_0 = 0$ (Albergo & Vanden-Eijnden, 2023; Ma et al., 2024). For readability, we remove the dependence of $\boldsymbol{x}_t$ on t when there is no ambiguity. The interpolation Eq. (2) is the forward process of flow matching, whose dynamics can be represented by the probability flow ODE (Ma et al., 2024)

$$\dot{\boldsymbol{x}} = \boldsymbol{v}_t(\boldsymbol{x}). \tag{3}$$

Here, the velocity field $\boldsymbol{v}$ satisfies

$$\boldsymbol{v}_t(x) = \mathbb{E}(\dot{\boldsymbol{x}}_t | \boldsymbol{x}_t = x) = \dot{\alpha}_t \mathbb{E}(\boldsymbol{x}_0 | \boldsymbol{x}_t = x) + \dot{\sigma}_t \mathbb{E}(\boldsymbol{x}_T | \boldsymbol{x}_t = x). \tag{4}$$

Typically, the velocity is parameterized by a neural net $\boldsymbol{v}_\theta$ and trained by minimizing the loss

$$\mathcal{L}_{\boldsymbol{v}}(\theta) = \int_0^T \mathbb{E}\|\boldsymbol{v}_{t,\theta}(\boldsymbol{x}) - \dot{\alpha}_t \boldsymbol{x}_0 + \dot{\sigma}_t \boldsymbol{x}_T\|^2 dt. \tag{5}$$

Given a sufficiently well trained $\boldsymbol{v}_\theta$, one can sample the target $\boldsymbol{x}^*$ by numerically solving Eq. (3) in reverse time, i.e.,

$$\dot{\boldsymbol{x}} = -\boldsymbol{v}_t(\boldsymbol{x}), \tag{6}$$

with initial condition $\boldsymbol{x}_T = \boldsymbol{\varepsilon}_x$. This corresponds to the reverse process of flow matching.

In contrast to flow matching, diffusion models directly define the dynamics of the forward process through an SDE. Given certain choices of the drift and diffusion coefficients, the forward process converges to a noise distribution. More specifically, the forward diffusion model corresponds to the Ito process

$$d\boldsymbol{x} = \boldsymbol{f}(\boldsymbol{x}, t)dt + g(t)d\boldsymbol{W}, \tag{7}$$

where $\boldsymbol{f}$ and g are predetermined, and $\boldsymbol{W}$ denotes standard Brownian motion. Specific choices of $\boldsymbol{f}$ and g lead to different diffusion models. For example, taking $\boldsymbol{f}(\boldsymbol{x}, t) = -\frac{1}{2}\beta(t)\boldsymbol{x}$ and $g(t) = \sqrt{\beta(t)}$ for some $\beta(t) > 0$, we obtain the variance-preserving (VP) SDE (Song et al., 2021b; Ho et al., 2020)

$$d\boldsymbol{x} = -\frac{1}{2}\beta(t)\boldsymbol{x}dt + \sqrt{\beta(t)}d\boldsymbol{W}. \tag{8}$$

When $T \to \infty$, the noise $\boldsymbol{x}_T \sim \mathcal{N}(0, \boldsymbol{I})$.

The reverse process of Eq. (7) was shown (Anderson, 1982) to correspond to

$$\mathrm{d}\boldsymbol{x} = \left[\boldsymbol{f}(\boldsymbol{x}, t) - g(t)^2 \boldsymbol{s}_t(\boldsymbol{x})\right] \mathrm{d}t + g(t)\mathrm{d}\overline{\boldsymbol{W}}, \tag{9}$$

where $\overline{\boldsymbol{W}}$ is a Brownian motion independent of $\boldsymbol{W}$, and $\boldsymbol{s}_t(\boldsymbol{x})$ denotes the score function of $\boldsymbol{x}_t$. Using the forward process defined in Eq. (8), one trains a neural net to learn the score function $\boldsymbol{s}_{t,\theta}(\boldsymbol{x}) \approx \nabla_x \log p(\boldsymbol{x}, t)$ via a loss similar to Eq. (5), where $p(\boldsymbol{x}, t)$ is the PDF of $\boldsymbol{x}_t$. One then runs the reverse process detailed in Eq. (9) with the trained score to obtain a data sample (Song et al., 2021b).

2.2 Relation between Flow Matching and Diffusion Models

There are both common grounds and differences between flow matching and diffusion models. For the flow matching setting, Ma et al. (2024) shows that

$$\boldsymbol{v}_t(\boldsymbol{x}) = a_t \boldsymbol{x} + b_t \boldsymbol{s}_t(\boldsymbol{x}), \tag{10}$$

where a_t, b_t are determined by α_t and σ_t in Eq. (2), demonstrating the fact that score and velocity are interchangeable. However, it can also be shown by Tweedie's formula (Efron, 2011) that

$$\boldsymbol{s}_t(\boldsymbol{x}_t) = -\alpha_t^{-1}\mathbb{E}(\boldsymbol{x}_0|\boldsymbol{x}_t), \tag{11}$$

which reveals a singularity in the score function at time T, since $\alpha_T = 0$. As $\boldsymbol{v}$ does not explode so long as the interpolation coefficients are smooth, training a velocity via flow matching is numerically more stable than training the score.

Though score and velocity are closely related, diffusion and flow matching models still differ significantly in terms of dynamics. In flow matching, there is only one noise variable $\boldsymbol{\varepsilon}_x$. Interpolation between data and noise leaves the path-wise trajectory of $\boldsymbol{x}_{[0,T]}$ smooth in t. In contrast, diffusion models are driven by Brownian motion, such that the path-wise trajectory is non-differentiable. Therefore, the law of a diffusion process and a flow matching process can never agree. Nevertheless, with certain choices of coefficients, a flow matching model and a diffusion model can share the same marginal distributions. For example, consider the VP SDE given in Eq. (8). Let $T = \infty$, $\alpha_t = \sqrt{1 - e^{-\int_0^t \beta(s)ds}}$, and $\sigma_t = e^{-\frac{1}{2}\int_0^t \beta(s)ds}$. Then the distribution of $\boldsymbol{x}_t$ generated by Eq. (2) is exactly the same as the one of the VP SDE given in Eq. (8). This suggests that a number of algorithms such as DPS (Chung et al., 2023b) can replace their diffusion based priors with flow matching priors, since it is often the marginal distribution instead of the law of the whole process that matters.

2.3 Linear inverse problems with flow matching and diffusion prior

Recent attempts addressing linear inverse problems using flow matching or diffusion models can be classified into two categories: 1) task-specific methods that train a conditional diffusion model (Saharia et al., 2023; 2022; Whang et al., 2022); and 2) task-agnostic methods that only rely on pre-trained unconditional diffusion models. For task specific methods, Liu et al. (2023a); Chung et al. (2023c) formulate the conditional diffusion as a Schrödinger bridge problem, which can be further related to the Doob's h-transform (Särkkä & Solin, 2019; Zhang et al., 2021) and stochastic optimal control (Uehara et al., 2024).

Task-agnostic methods tackle Bayesian inverse problems, where pre-trained flow matching or diffusion models are treated as priors. In contrast to the usual Bayesian settings, the prior can only be sampled by solving the reverse process. The key question is how to incorporated measurement likelihood into the reverse process such that it leads to a solution of the problem. Ideally, one method is to "hijack" the reverse process by adding a guidance such that the process is conditioned on the measurement $\boldsymbol{y}$. For instance, for diffusion priors, one aims to sample from the following SDE:

$$\mathrm{d}\boldsymbol{x} = \left[\boldsymbol{f}(\boldsymbol{x}, t) + g(t)^2 \nabla_{\boldsymbol{x}} \log p_t\left(\boldsymbol{x}|\boldsymbol{y}\right)\right] \mathrm{d}t + g(t)\mathrm{d}\boldsymbol{W}. \tag{12}$$

Since $\nabla_{\boldsymbol{x}_t} \log p_t\left(\boldsymbol{x}_t|\boldsymbol{y}\right) = \nabla_{\boldsymbol{x}} \log p_t\left(\boldsymbol{x}_t\right) + \nabla_{\boldsymbol{x}} \log q\left(\boldsymbol{y}|\boldsymbol{x}_t\right)$ (Bayes rule), $\nabla_{\boldsymbol{x}} \log q\left(\boldsymbol{y}|\boldsymbol{x}_t\right)$ is the guidance leading to the posterior. However, the conditional density $q\left(\boldsymbol{y}|\boldsymbol{x}_t\right)$ is intractable, because the measurement $\boldsymbol{y}$ only depends on $\boldsymbol{x}_0 = \boldsymbol{x}^*$ due to the linear inverse problem specified in Eq. (1).

Though the likelihood is intractable, various algorithms have been proposed to tackle linear inverse problems with diffusion or flow matching prior. Among the existing methods, Chung & Ye (2022); Chung et al. (2022); Zhu et al. (2023) adopt a projection onto the measurement subspace; Kawar et al. (2022); Meng & Kabashima (2022) approximate $q(\boldsymbol{y}|\boldsymbol{x}_t)$ via SVD; Mardani et al. (2024); Feng et al. (2023) use variational inference; Fei et al. (2023); Chung et al. (2023b); Song et al. (2023); Pokle et al. (2023); Pandey et al. (2024) estimate the likelihood score $\nabla_{\boldsymbol{x}_t} \log q(\boldsymbol{y}|\boldsymbol{x}_t)$; Dou & Song (2024); Trippe et al. (2023); Cardoso et al. (2024) carry out exact Bayesian posterior estimation with sequential Monte Carlo (SMC); Choi et al. (2021); Song et al. (2022) enforce data consistency via optimization at each time step; Ben-Hamu et al. (2024) optimize the starting noise so that the generation process yields the intended results; Xu & Chi (2024); Li et al. (2024) use the variable splitting techniques (Geman & Yang, 1995; Afonso et al., 2010; Boyd et al., 2011; Venkatakrishnan et al., 2013) to decouple the optimization with respect to prior and data consistency; Zhang et al. (2024) introduce a decoupled noise annealing process to handle highly nonlinear problems. Despite promising experimental results, we find prior works struggle to efficiently handle challenging linear inverse problems. More specifically, we find methods of high reconstruction quality are often time consuming, and efficient methods fail to consistently obtain high quality reconstruction throughout different tasks. Furthermore, none of the existing methods are able to handle challenging scenarios like high measurement noise.

3 METHOD

In this section, we propose 'Flow with Interpolant Guidance' (FIG), a simple yet effective algorithm that can leverage all pre-trained flow matching and diffusion models to solve linear inverse problems. During initialization, we perturb the measurement $\{\boldsymbol{y}\}_{t\in[0,T]}$ parallel to the forward process of $\boldsymbol{x}$ to get measurement interpolants $\boldsymbol{y}_t$ similar to (Song et al., 2022). The intuition if measurement interpolants comes from filtering (Dou & Song, 2024), and it ensures that for all t, the likelihood $q_t(\boldsymbol{y}_t|\boldsymbol{x}_t)$ is Gaussian. Then at each time $t \in [0, T]$, we incorporate $q_t(\boldsymbol{y}_t|\boldsymbol{x}_t)$ as guidance for sampling $\boldsymbol{x}_t$. This section provides more details and is organized as follows. In Section 3.1, we state how to obtain measurement interpolants. Section 3.2 presents the FIG algorithm. We then show in Section 3.3 that the updating scheme is theoretically justified. Section 3.4 discusses details regarding the practical implementation of our algorithm. For readability, we choose to adopt a flow matching narrative in most of this section, although FIG can also use a diffusion prior. Empirical results using both flow matching and diffusion priors will be shown in Section 4.

3.1 GENERATING MEASUREMENT INTERPOLANTS

Given a pre-trained flow model, $\boldsymbol{x}_t$ is interpolated following Eq. (2), with $\boldsymbol{x}_0$ following the data distribution and $\boldsymbol{x}_T = \boldsymbol{\varepsilon}_x \sim \mathcal{N}(0, \boldsymbol{I})$. We consider a parallel interpolation of $\boldsymbol{y}$, i.e.,

$$\boldsymbol{y}_t = \alpha_t \boldsymbol{y}_0 + \sigma_t \boldsymbol{y}_T, \tag{13}$$

where $\boldsymbol{y}_0 = \boldsymbol{y}$, and $\boldsymbol{y}_T = \boldsymbol{\varepsilon}_y = \boldsymbol{A}\boldsymbol{\varepsilon}_x$. The following sequence of equalities reveals the distribution of $q_t(\boldsymbol{y}_t|\boldsymbol{x}_t)$:

$$\boldsymbol{y}_t = \alpha_t(\boldsymbol{A}\boldsymbol{x}_0 + \boldsymbol{n}) + \sigma_t \boldsymbol{A}\boldsymbol{\varepsilon}_x = \boldsymbol{A}(\alpha_t \boldsymbol{x}_0 + \sigma_t \boldsymbol{x}_T) + \alpha_t \boldsymbol{n} = \boldsymbol{A}\boldsymbol{x}_t + \alpha_t \boldsymbol{n}. \tag{14}$$

Hence, we have $q_t(\boldsymbol{y}_t|\boldsymbol{x}_t) = \mathcal{N}\left(\boldsymbol{y}_t; \boldsymbol{A}\boldsymbol{x}_t, \alpha_t^2 \sigma_n^2 \boldsymbol{I}\right)$. We note that the generation of the process $\boldsymbol{y}_t$ relies on the fact that the measurement $\boldsymbol{y}_0$ has a linear relationship with the signal $\boldsymbol{x}_0$, thus the interpolant measurement only works for linear models.

Algorithm 1 Flow with Interpolant Guidance (FIG)

Require: T, c, K, w, $\boldsymbol{y}_0$
1: Initialize $\boldsymbol{x}_T = \boldsymbol{\varepsilon}_x \sim \mathcal{N}(\mathbf{0}, \boldsymbol{I})$ ▷ Initialize $\boldsymbol{x}_t$
2: $\Delta t = 1/T$
3: **for** $i = T$ **to** 1 **do**
4: $t = i/T, t' = (i-1)/T$
5: $\boldsymbol{y}_{i-1} = \alpha_{t'}\boldsymbol{y}_0 + w\sigma_{t'}\boldsymbol{A}\boldsymbol{\varepsilon}_x$ ▷ measurement interpolation with rescaled variance
6: $\boldsymbol{x}_{i-1} = \boldsymbol{x}_i - \boldsymbol{v}_\theta(\boldsymbol{x}_i, t)\Delta t$ ▷ Unconditional update
7: **for** $k = 1$ **to** K **do**
8: $\boldsymbol{x}_{i-1} = \boldsymbol{x}_{i-1} - \frac{c\lambda_t\sigma_t\Delta t}{2\alpha_t^2\sigma_n^2}\nabla_{\boldsymbol{x}_{i-1}}\|\boldsymbol{y}_{i-1} - \boldsymbol{A}\boldsymbol{x}_{i-1}\|_2^2$ ▷ K-times conditional update
9: **end for**
10: **end for**

It is worth mentioning that $\boldsymbol{x}_t$ in Eq. (14) is defined by the interpolation process given in Eq. (2), instead of the probability flow ODE detailed in Eq. (3). In this case it is fair to ask: is the conditional distribution of $\boldsymbol{y}_t|\boldsymbol{x}_t$ still Gaussian when $\boldsymbol{x}_t$ is sampled from Eq. (3)? The answer is yes because $\boldsymbol{x}_t$ defined in Eq. (2) and Eq. (3) have the same distribution (Liu et al., 2023b).

3.2 Algorithm Overview

Before diving into the detailed analysis, we first provide an overview of the FIG algorithm (see Algorithm 1). The algorithm numerically solves a reverse-time ODE to generate samples from the correct posterior,

$$d\boldsymbol{x} = -\boldsymbol{v}_t(\boldsymbol{x})dt + \lambda_t\sigma_t\nabla_x \log q_t(\boldsymbol{y}_t|\boldsymbol{x})dt, \quad \text{with} \quad \boldsymbol{x}_T \sim \mathcal{N}(0, \boldsymbol{I}). \tag{15}$$

Here, $\boldsymbol{v}_t$ denotes the (unconditional) velocity field from the pre-trained model, $\lambda_t = \dot{\sigma}_t - \frac{\dot{\alpha}_t}{\alpha_t}\sigma_t$, and $\nabla_x \log q_t(\boldsymbol{y}|\boldsymbol{x}) = -\frac{1}{2\alpha_t^2\sigma_n^2}\nabla_x\|\boldsymbol{y} - \boldsymbol{A}\boldsymbol{x}\|^2$. The derivation and justification of Eq. (15) are detailed in Section 3.3.

Numerically, time is discretized on a uniform grid with Δt referring to the step size. In the following, we use $\boldsymbol{x}_i$ and $\boldsymbol{y}_i$ instead of $\boldsymbol{x}_{t_i}$ and $\boldsymbol{y}_{t_i}$ for readability. The updating scheme at each time t_i, corresponding to an Euler's method with splitting (Leimkuhler & Matthews, 2015), is as follows:

$$\begin{cases} \boldsymbol{x}'_{i-1} &= \boldsymbol{x}_i - \boldsymbol{v}_{t_i}(\boldsymbol{x}_i)\Delta t \\ \boldsymbol{x}_{i-1} &= \boldsymbol{x}'_{i-1} - \frac{\lambda_t\sigma_t}{2\alpha_t^2\sigma_n^2}\nabla_{x'_{i-1}}\|\boldsymbol{y}_{i-1} - \boldsymbol{A}\boldsymbol{x}'_{i-1}\|^2\Delta t. \end{cases} \tag{16}$$

Each step of the two-step updating scheme has a different aim. The first step in Eq. (16) corresponds to the unconditional update, which is exactly a numerical discretization of the reverse process specified in Eq. (6). In a practical implementation it is performed via Euler's method (see line 6 in Algorithm 1). The second step is a conditional update that incorporates measurement information. In practice K gradient descent steps with learning rate c carry out the conditional update (see line 7 to line 9 in Algorithm 1). We introduce the theoretical reasoning of this simple but effective updating scheme next.

3.3 Theoretical justification

We now provide the theoretical reasoning underlying FIG. Importantly, note that for all $t \in (0, T)$, the marginal distribution of $\boldsymbol{y}_t$ is uniquely determined by $\boldsymbol{y}_0$ and $\boldsymbol{\varepsilon}_y$ as detailed in Eq. (13). We make the following technical assumption:

Assumption 1 *The conditional distribution of $\boldsymbol{x}_t$ given $\boldsymbol{y}_0$ and $\boldsymbol{\varepsilon}_y$ is equivalent to the conditional distribution of $\boldsymbol{x}_t$ given $\boldsymbol{y}_t$.*

Let $p_t(\cdot|\boldsymbol{y}_t)$ be the density of $\boldsymbol{x}_t$ given $\boldsymbol{y}_t$. The following theorem reviews the dynamics of $p_t(\cdot|\boldsymbol{y}_t)$.

Theorem 1 *Let $\boldsymbol{v}_t(\boldsymbol{x}|\boldsymbol{y}_t)$ be the conditional velocity field that generates p_t, i.e., $p_t(\boldsymbol{x}|\boldsymbol{y}_t)$ solves the reverse-time continuity equation with initial condition p_T being a standard Gaussian:*

$$\partial_t p_t(\boldsymbol{x}|\boldsymbol{y}_t) - \nabla_x \cdot [\boldsymbol{v}_t(\boldsymbol{x}|\boldsymbol{y}_t)p_t(\boldsymbol{x}|\boldsymbol{y}_t)] = 0. \tag{17}$$

Let $\boldsymbol{s}_t(\boldsymbol{x}|\boldsymbol{y}_t) = \nabla_x \log p_t(\boldsymbol{x}|\boldsymbol{y}_t)$ be the score function. Then under Assumption 1,

$$\boldsymbol{v}_t(\boldsymbol{x}|\boldsymbol{y}_t) = \frac{\dot{\alpha}_t}{\alpha_t}\boldsymbol{x} - \lambda_t \sigma_t \boldsymbol{s}_t(\boldsymbol{x}|\boldsymbol{y}_t). \tag{18}$$

We defer the proof to Appendix A.1. Theorem 1 describes the conditional dynamics, which demonstrates consistency. The corresponding (reverse-time) probability flow ODE gives rise to the numerical updating scheme Eq. (16):

$$d\boldsymbol{x} = -\boldsymbol{v}_t(\boldsymbol{x}|\boldsymbol{y}_t)dt, \tag{19}$$

with initial condition $\boldsymbol{x}_T \sim \mathcal{N}(0, \boldsymbol{I})$. In view of Eq. (18), we rewrite the conditional probability flow ODE detailed in Eq. (19) as

$$\begin{aligned} d\boldsymbol{x} &= -\boldsymbol{v}_t(\boldsymbol{x}|\boldsymbol{y}_t)dt = -\Big(\frac{\dot{\alpha}_t}{\alpha_t}\boldsymbol{x} - \lambda_t\sigma_t\nabla_x \log p_t(\boldsymbol{x}|\boldsymbol{y}_t)\Big)dt \\ &= -\Big(\frac{\dot{\alpha}_t}{\alpha_t}\boldsymbol{x} - \lambda_t\sigma_t\nabla_x \log p_t(\boldsymbol{x})\Big)dt + \lambda_t\sigma_t\nabla_x \log q_t(\boldsymbol{y}_t|\boldsymbol{x})dt \\ &= -\boldsymbol{v}_t(\boldsymbol{x})dt + \lambda_t\sigma_t\nabla_x \log q_t(\boldsymbol{y}_t|\boldsymbol{x})dt. \end{aligned} \tag{20}$$

Here, $\nabla_x \log q_t(\boldsymbol{y}|\boldsymbol{x}) = -\frac{1}{2\alpha_t^2\sigma_n^2}\nabla_x\|\boldsymbol{y}-\boldsymbol{A}\boldsymbol{x}\|^2$. Further, $\boldsymbol{v}_t$ denotes the (unconditional) velocity field from the pre-trained model. Note that this equation is identical to Eq. (15). An Euler discretization of Eq. (15) yields exactly Eq. (16). Interestingly, when we let $\alpha_t = 1 - t$ and $\sigma_t = t$, i.e., when we follow the rectified flow (Liu et al., 2023b), the coefficient $\lambda_t\sigma_t = \frac{t}{1-t} = 1/\text{SNR}_t$, where $\text{SNR}_t = \frac{1-t}{t} = \frac{\alpha_t}{\sigma_t}$. The following corollary summarizes the direction of the conditional update.

Corollary 1 *The conditional update direction at time t_i is equivalent to a gradient flow direction that maximizes an $\mathcal{L}_2$-regularized posterior log-likelihood at the next timestep $\log p_{i-1}(\boldsymbol{x}_{i-1}|\boldsymbol{y}_{i-1})$:*

$$\nabla_{x_{i-1}}\Big(\log p_{i-1}(\boldsymbol{x}_{i-1}|\boldsymbol{y}_{i-1}) + \frac{|\dot{\alpha}_{i-1}|}{\alpha_{i-1}}\frac{1}{SNR_t}\frac{\|\boldsymbol{x}_{i-1}\|^2}{2}\Big). \tag{21}$$

Corollary 1 demonstrates that FIG updating direction is equivalent to maximizing a regularized log-likelihood, providing further intuition into the algorithm. The proof is provided in Appendix A.2.

While all previous derivations uses a flow matching base model, FIG can also be applied to diffusion models. When adopting a diffusion prior, the following corollary states the SDE version of FIG.

Corollary 2 *Let the pre-trained unconditional generation be a diffusion model, as detailed in Eq.* (7)*, then FIG admits the form:*

$$\mathrm{d}\boldsymbol{x} = \left[\boldsymbol{f}(\boldsymbol{x}, t) + g(t)^2\boldsymbol{s}_t\left(\boldsymbol{x}|\boldsymbol{y}_t\right)\right]\mathrm{d}t + g(t)\mathrm{d}\overline{\boldsymbol{W}}. \tag{22}$$

Numerically sampling Eq. 22 gives the FIG algorithm with diffusion prior. It is interesting to observe that Eq. (22) coincides with the limiting process of FPS (Dou & Song, 2024), yet the sampling procedure of FIG remains different. The proof is given in Appendix A.3.

3.4 Practical Implementation

In practice, we observe that a conditional update can be viewed as minimizing the distance between the data $\boldsymbol{x}_t$ projected onto the measurement space and the measurement interpolants $\boldsymbol{y}_t$. The likelihood score represents the gradient of the conditional update. Therefore, a single conditional update corresponds to one step of gradient descent. If we perform only one conditional update per timestep and adjust the update magnitude solely by tuning the weight c of the likelihood score, the effectiveness of the conditional update within a single timestep will be significantly reduced. However, if fully optimizing this distance, the log-likelihood of measurement interpolant will be overwhelming compared to the prior information, resulting in severe overfitting. Thus, maintaining a balance between the measurement information and the prior information is crucial for our reconstruction problem. To remedy the issue, we introduce a new parameter K. After an unconditional update, we perform K conditional updates with theoretically justified weights and directions as previously shown. We also note that due to the nature of ODEs, once the velocity field and initialization are

Method	SR (4×)			Gaussian Deblur			Motion Deblur			Inpainting		
	PSNR ↑	SSIM ↑	LPIPS ↓	PSNR ↑	SSIM ↑	LPIPS ↓	PSNR ↑	SSIM ↑	LPIPS ↓	PSNR ↑	SSIM ↑	LPIPS ↓
FIG-Flow	**29.41**	**0.811**	**0.201**	**26.83**	**0.738**	0.261	**30.84**	**0.871**	**0.209**	**27.08**	**0.814**	0.274
DPS-Flow	28.73	0.777	0.221	22.95	0.568	0.337	21.95	0.571	0.382	27.05	0.801	**0.244**
DMPS	29.00	0.807	0.222	26.74	0.725	0.255	29.81	0.828	0.226	12.66	0.284	0.658
OT-ODE	28.40	0.769	0.225	26.34	0.708	**0.252**	29.07	0.818	0.226	18.86	0.475	0.500
FIG-Diffusion	**29.89**	**0.846**	0.163	**29.83**	**0.845**	0.147	**31.81**	**0.882**	0.137	27.36	**0.848**	**0.163**
DPS-Diffusion	28.85	0.801	0.172	28.32	0.797	**0.136**	30.69	0.843	0.127	28.23	0.793	0.164
DDNM+	28.82	0.750	0.340	7.84	0.021	0.840	-	-	-	**28.70**	0.843	0.182
DAPS	29.59	0.809	0.158	29.74	0.808	0.146	31.67	0.859	**0.119**	27.85	0.791	0.183
C-ΠGDM	28.14	0.787	**0.106**	3.72	0.077	0.860	-	-	-	13.28	0.216	0.729

Table 1: Quantitative comparison (PSNR, SSIM, LPIPS) of different algorithms for different tasks on the CelebA-HQ 256×256 test dataset. All input images have a measurement Gaussian noise of $\sigma_n = 0.05$. **Bold** for the best.

determined, the final generated data is uniquely determined. However, the random initialization does not correspond to the desired reconstruction result. Therefore, we opt to average multiple random initializations, thereby reducing the impact of incorrect initial values during the interpolation of measurements. Given that our measurement model is linear, this approach is equivalent to introducing another parameter w to generate $\boldsymbol{y}_t$, i.e., the new $\boldsymbol{y}_t$ is generate via $\alpha_t \boldsymbol{y}_0 + w\sigma_t \boldsymbol{\varepsilon}_y$.

By combining the practical design considerations, we obtain Algorithm 1. The parameters c, w, K are constants, with c and K being task-specific, governing the balance between unconditional and conditional updates. The parameter w helps us obtain an empirically better log-likelihood of the measurement interpolants. The effectiveness of both strategies is examined in later ablation studies.

Though FIG is effective in solving most linear inverse problems for imaging, it struggles with inpainting tasks where a large region is masked. The reason is that the masked pixels carry zero information for the conditional update, as they are totally "masked". Therefore, we propose a simple remedy termed FIG+. It improves the performance for inpainting tasks. Concretely, for each $\boldsymbol{x}_t$ update, we first estimate $\hat{\boldsymbol{x}}_0$ using Tweedie's formula, and perturb it to time t to get $\hat{\boldsymbol{x}}_t$. Then we mix the masked parts of $\hat{\boldsymbol{x}}_t$ with the current $\boldsymbol{x}_t$ to update the masked region. A hyper-parameter mixing weight $m \in [0, 1]$ determines how much we trust $\hat{\boldsymbol{x}}_0$. We provide the pseudocode in Appendix B. When $m = 0$, we retrieve the original FIG algorithm. The added three lines compared to the original FIG algorithm only involve simple addition and matrix (mask) multiplication. Hence they don't affect the runtime and memory consumption much. In our experiments below, we only use FIG+ for the inpainting task.

4 Experiments

4.1 Experimental Setup

Datasets. We conduct experiments on 3 natural image datasets: CelebA-HQ (Karras et al., 2018), LSUN-Bedroom (Yu et al., 2015), and AFHQ-Cat (Choi et al., 2020). All images used are from the official test splits and preprocessed to the size of $256 \times 256 \times 3$.

Tasks. Our evaluation focuses on linear inverse problems including super-resolution, deblurring, and inpainting. For super-resolution, we apply $4\times$ bicubic downsampling across all datasets. For deblurring tasks, we use Gaussian blurring with a kernel size of 61×61 and a standard deviation of 3.0, and motion blurring with the same kernel size but a standard deviation of 0.5. For inpainting, we perform random inpainting by masking out 90% of the total pixels. We follow the SVD-based measurement operations defined in DDRM (Kawar et al., 2022), as DDNM, DMPS, and OT-ODE require an SVD for their conditional updates. For all tasks above, we add a measurement Gaussian noise $\boldsymbol{n} \sim \mathcal{N}(\mathbf{0}, \sigma_n^2 \boldsymbol{I})$ with $\sigma_n = 0.05$. To further demonstrate the capabilities of our algorithm, we conducted two additional, more complex experiments: $4\times$ super-resolution with high noise ($\sigma_n = 1.0$), $16\times$ super-resolution with noise ($\sigma_n = 0.2$).

(a) Reference (b) Measure (c) DPS (d) DMPS (e) OT-ODE (f) FIG (ours)

Figure 2: Results for 90% random inpainting with noise $\sigma_n = 0.05$ on the CelebA-HQ dataset using a flow matching base model.

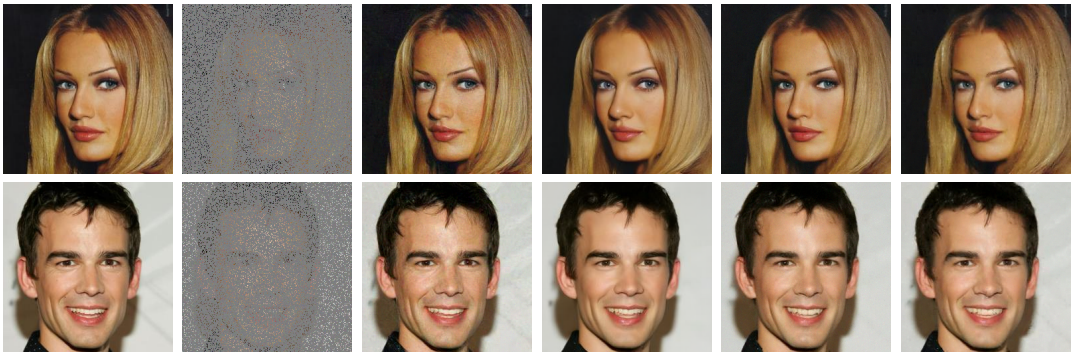

(a) Reference (b) Measure (c) DPS (d) DDNM+ (e) DAPS (f) FIG (ours)

Figure 3: Results for 90% random inpainting with noise $\sigma_n = 0.05$ on the CelebA-HQ dataset using a diffusion base model.

Metrics. For the quantitative comparison, we use the perceptual Learned Perceptual Image Patch Similarity (LPIPS) distance (Zhang et al., 2018), along with two standard metrics: peak signal-to-noise-ratio (PSNR), and structural similarity index (SSIM).

Baselines. We compare the performance of our algorithm to several state-of-the-art training-free algorithms for solving inverse problems, including DPS (Chung et al., 2023b), OT-ODE (Pokle et al., 2023), DMPS (Meng & Kabashima, 2022), DDNM/DDNM+ (Wang et al., 2023), DAPS (Zhang et al., 2024), and C-ΠGDM (Pandey et al., 2024). OT-ODE is an improved version of ΠGDM (Song et al., 2023) applied to flow matching models, thus it is used instead of ΠGDM as the baseline. Likewise, we transferred DPS and DMPS to flow matching using Eq. (18). Leveraging the advantages of flow matching models, we fine-tune the baseline methods to ensure they all achieve their best performance at 50 NFEs except for OT-ODE. It requires less than 50 NFEs due to its start time strategy.

Base Models. We implemented our FIG algorithm for both flow matching and diffusion models. We refer to both incarnations via FIG-Flow and FIG-Diffusion. For each base model, we then compared with three state-of-the-art algorithms respectively. For FIG-Flow, we use the pre-trained Rectified Flow model from Liu et al. (2023b) as our base model and implement all baselines on it to ensure a fair comparison. In the diffusion category, we utilize EDM (Karras et al., 2022) as the base model for our algorithm, DPS, and DAPS. Since DDNM/DDNM+ employs a unique time travel structure that may not transfer well, we retain their original DDIM base model and conduct experiments using their original code. For C-ΠGDM, we use the default VPSDE (Song et al., 2021b). For unconditional generation, we choose the Euler ODE solver for simplicity as it makes it easier to add the measurement information at each sampling step.

4.2 Experimental Results

The quantitative comparisons are listed in Tables 1, 2, 11 and 12, with samples of reconstructed images shown in Figs. 2 to 6. Additional experimental results are presented in Appendices F and G. Our

Method	SR (4×) $\sigma_n = 1.0$			SR(16×) $\sigma_n = 0.2$		
	PSNR ↑	SSIM ↑	LPIPS ↓	PSNR ↑	SSIM ↑	LPIPS ↓
FIG (ours)	**24.47**	**0.722**	**0.315**	**19.92**	**0.553**	**0.405**
DPS	22.50	0.593	0.378	19.20	0.531	0.424
DMPS	24.06	0.678	0.342	19.91	0.536	0.441
OT-ODE	15.14	0.191	0.695	17.79	0.408	0.570

Table 2: Quantitative comparison (PSNR, SSIM, LPIPS) of different algorithms for high noise bicubic super-resolution on the CelebA-HQ 256 × 256 test dataset. **Bold** for the best.

(a) Reference (b) Measure (c) DPS (d) DMPS (e) OT-ODE (f) FIG (ours)

Figure 4: Results for 4× bicubic super-resolution with high noise $\sigma_n = 1.0$ on the CelebA-HQ dataset.

algorithm FIG demonstrates highly competitive performance across all tasks, metrics, and datasets. For all these tasks, DPS and OT-ODE tend to produce sharper edges, but this sometimes results in unrealistic details and textures, leading to worse metrics. In contrast, our algorithm generates faithfully smooth images with a good balance of detail and realism.

Our algorithm exhibits superior performance compared to other baselines with flow matching prior, particularly for the challenging super-resolution tasks with high levels of noise. We do not include the results from diffusion-based algorithms for those tasks because they all fail to yield a reasonable reconstruction. Note that Wang et al. (2023) reported a similar task with average pooling super-resolution but it fails on bicubic super-resolution. See Appendix E for more details of DDNM/DDNM+. Additionally, to further demonstrate the robustness of our algorithm, we test it on 4× super-resolution with non-uniform and high noise. As shown in Fig. 6, our algorithm performs well even under these challenging conditions.

Algorithm	Total Memory	NFEs	Avg. Inf. Time (s)
FIG-Flow	**7735MB**	50	**2.80±0.12**
DPS-Flow	8109MB	50	4.41±0.14
DMPS	7847MB	50	2.83±0.15
OT-ODE	8257MB	40	3.69±0.14
FIG-Diffusion	**2809MB**	100	4.06±1.01
DPS-Diffusion	7761MB	100	8.19±1.04
DDNM+	28707MB	1210	28.36±0.61
DAPS	**2809MB**	1000	59.56±1.70
C-ΠGDM	5697MB	5	**0.45±0.01**

Table 3: The running time and memory consumption required for different algorithms on the CelebA-HQ 256×256 test dataset for the super-resolution task. All experiments are conducted on a single NVIDIA RTX A6000 GPU for reconstruction of one image. **Bold** for the best.

In addition to the outstanding performance, our algorithm is highly efficient in terms of computational resources as shown in Table 3. For the same NFEs (except for OT-ODE due to its initialization technique), our algorithm attains optimal results in both running time and memory usage.

To validate our theoretical results and the effectiveness of practical design components, we perform ablation studies (detailed in Appendix C) on 1) K-times conditional update with results in Fig. 7

(a) Reference (b) Measure (b) DPS (b) DMPS (b) OT-ODE (b) FIG (ours)

Figure 5: Results for $16\times$ bicubic super-resolution with high noise $\sigma_n = 0.2$ on the CelebA-HQ dataset.

(a) Reference (b) Measure (c) FIG (ours) (d) Reference (e) Measure (f) FIG (ours)

Figure 6: Results for $16\times$ bicubic super-resolution with high non-uniform Gaussian noise (first row) and non-uniform Laplacian noise (second row) on CelebA-HQ dataset.

and Tables 4 to 6 in Appendix C.1; 2) measurement interpolant variance rescaling with results in Fig. 8 and Tables 7 to 9 in Appendix C.2. Both the visual outputs and quantitative results support the principles underlying the development of FIG.

5 Conclusion

In this paper, we presented FIG, a task-agnostic algorithm for solving linear inverse problems. Our key observation: adding noise to the measurement is easier compared to denoising the signal. We thus use measurement interpolants to guide the unconditional generation. The FIG algorithm is simple yet effective, as is shown by experiments on multiple tasks over several high-dimensional datasets.

Limitations: First, since the measurement interpolants rely on the linear relationship between the measurement and the underlying signal, FIG can not directly be applied to general non-linear inverse problems. For the same reason, the algorithm is not compatible with pre-trained models with latent encodings. Second, the FIG result is still an approximated posterior. To obtain true posterior samples, one should consider methods based on stochastic optimal control (Guo et al., 2024; Uehara et al., 2024). Another way is to sequentially update ε_x so that it generates the intended image (Ben-Hamu et al., 2024).

Future Work: Although FIG can not be extended to non-linear problems in general, its potential application in bilinear problems such as blind motion deblurring (Chung et al., 2023a; Fei et al., 2023) could be an interesting direction. When fixing either the blurring kernel or the image, the noise model is linear, thus measurement interpolants can be constructed. Using FIG's updating scheme consecutively would potentially lead to reconstruction. However, initialization and regularization on the kernel are highly non-trivial, and requires future explorations. Another interesting direction is to extend FIG to latent models (Rout et al., 2024; Song et al., 2024).

REFERENCES

Manya V Afonso, José M Bioucas-Dias, and Mário AT Figueiredo. Fast image recovery using variable splitting and constrained optimization. *IEEE transactions on image processing*, 19(9): 2345–2356, 2010.

Michael S. Albergo, Nicholas M. Boffi, and Eric Vanden-Eijnden. Stochastic interpolants: A unifying framework for flows and diffusions, 2023.

Michael Samuel Albergo and Eric Vanden-Eijnden. Building normalizing flows with stochastic interpolants. In *The Eleventh International Conference on Learning Representations*, 2023.

Brian DO Anderson. Reverse-time diffusion equation models. *Stochastic Processes and their Applications*, 12(3):313–326, 1982.

Heli Ben-Hamu, Omri Puny, Itai Gat, Brian Karrer, Uriel Singer, and Yaron Lipman. D-flow: Differentiating through flows for controlled generation, 2024.

Stephen Boyd, Neal Parikh, Eric Chu, Borja Peleato, Jonathan Eckstein, et al. Distributed optimization and statistical learning via the alternating direction method of multipliers. *Foundations and Trends® in Machine learning*, 3(1):1–122, 2011.

Gabriel Cardoso, Yazid Janati el idrissi, Eric Moulines, and Sylvain Le Corff. Monte carlo guided denoising diffusion models for bayesian linear inverse problems. In *The Twelfth International Conference on Learning Representations*, 2024.

Ricky TQ Chen, Yulia Rubanova, Jesse Bettencourt, and David K Duvenaud. Neural ordinary differential equations. *Advances in neural information processing systems*, 31, 2018.

Jooyoung Choi, Sungwon Kim, Yonghyun Jeong, Youngjune Gwon, and Sungroh Yoon. Ilvr: Conditioning method for denoising diffusion probabilistic models. In *2021 IEEE/CVF International Conference on Computer Vision (ICCV)*, pp. 14347–14356, 2021.

Yunjey Choi, Youngjung Uh, Jaejun Yoo, and Jung-Woo Ha. StarGAN v2: Diverse image synthesis for multiple domains. In *Proceedings of the IEEE/CVF conference on computer vision and pattern recognition*, pp. 8188–8197, 2020.

Hyungjin Chung and Jong Chul Ye. Score-based diffusion models for accelerated mri. *Medical image analysis*, 80:102479, 2022.

Hyungjin Chung, Byeongsu Sim, and Jong Chul Ye. Come-closer-diffuse-faster: Accelerating conditional diffusion models for inverse problems through stochastic contraction. In *2022 IEEE/CVF Conference on Computer Vision and Pattern Recognition (CVPR)*, pp. 12403–12412, 2022.

Hyungjin Chung, Jeongsol Kim, Sehui Kim, and Jong Chul Ye. Parallel diffusion models of operator and image for blind inverse problems. In *Proceedings of the IEEE/CVF Conference on Computer Vision and Pattern Recognition*, pp. 6059–6069, 2023a.

Hyungjin Chung, Jeongsol Kim, Michael Thompson Mccann, Marc Louis Klasky, and Jong Chul Ye. Diffusion posterior sampling for general noisy inverse problems. In *The Eleventh International Conference on Learning Representations*, 2023b.

Hyungjin Chung, Jeongsol Kim, and Jong Chul Ye. Direct diffusion bridge using data consistency for inverse problems. In *Thirty-seventh Conference on Neural Information Processing Systems*, 2023c.

Prafulla Dhariwal and Alexander Quinn Nichol. Diffusion models beat GANs on image synthesis. In A. Beygelzimer, Y. Dauphin, P. Liang, and J. Wortman Vaughan (eds.), *Advances in Neural Information Processing Systems*, 2021.

Zehao Dou and Yang Song. Diffusion posterior sampling for linear inverse problem solving: A filtering perspective. In *The Twelfth International Conference on Learning Representations*, 2024.

Bradley Efron. Tweedie's formula and selection bias. *Journal of the American Statistical Association*, 106(496):1602–1614, 2011.

Ben Fei, Zhaoyang Lyu, Liang Pan, Junzhe Zhang, Weidong Yang, Tianyue Luo, Bo Zhang, and Bo Dai. Generative diffusion prior for unified image restoration and enhancement. In *Proceedings of the IEEE/CVF Conference on Computer Vision and Pattern Recognition*, pp. 9935–9946, 2023.

Berthy T. Feng, Jamie Smith, Michael Rubinstein, Huiwen Chang, Katherine L. Bouman, and William T. Freeman. Score-based diffusion models as principled priors for inverse imaging. In *2023 IEEE/CVF International Conference on Computer Vision (ICCV)*, pp. 10486–10497, 2023.

Donald Geman and Chengda Yang. Nonlinear image recovery with half-quadratic regularization. *IEEE transactions on Image Processing*, 4(7):932–946, 1995.

Yingqing Guo, Hui Yuan, Yukang Yang, Minshuo Chen, and Mengdi Wang. Gradient guidance for diffusion models: An optimization perspective. *arXiv preprint arXiv:2404.14743*, 2024.

Jonathan Ho, Ajay Jain, and Pieter Abbeel. Denoising diffusion probabilistic models. In *Advances in Neural Information Processing Systems*, volume 33, pp. 6840–6851, 2020.

Jérôme Idier. *Bayesian approach to inverse problems*. John Wiley & Sons, 2013.

Ajil Jalal, Marius Arvinte, Giannis Daras, Eric Price, Alex Dimakis, and Jonathan Tamir. Robust compressed sensing MRI with deep generative priors. In *Advances in Neural Information Processing Systems*, 2021.

Tero Karras, Timo Aila, Samuli Laine, and Jaakko Lehtinen. Progressive growing of GANs for improved quality, stability, and variation. In *International Conference on Learning Representations*, 2018.

Tero Karras, Miika Aittala, Timo Aila, and Samuli Laine. Elucidating the design space of diffusion-based generative models. In *Advances in Neural Information Processing Systems*, 2022.

Bahjat Kawar, Michael Elad, Stefano Ermon, and Jiaming Song. Denoising diffusion restoration models. In *ICLR Workshop on Deep Generative Models for Highly Structured Data*, 2022.

Benedict Leimkuhler and Charles Matthews. *Molecular Dynamics: With Deterministic and Stochastic Numerical Methods*. Interdisciplinary Applied Mathematics. Springer, 2015.

Xiang Li, Soo Min Kwon, Ismail R Alkhouri, Saiprasad Ravishanka, and Qing Qu. Decoupled data consistency with diffusion purification for image restoration. *arXiv preprint arXiv:2403.06054*, 2024.

Yaron Lipman, Ricky TQ Chen, Heli Ben-Hamu, Maximilian Nickel, and Matt Le. Flow matching for generative modeling. In *The Eleventh International Conference on Learning Representations*, 2023.

Guan-Horng Liu, Arash Vahdat, De-An Huang, Evangelos Theodorou, Weili Nie, and Anima Anandkumar. I^2SB: Image-to-image schrödinger bridge. In *Proceedings of the 40th International Conference on Machine Learning*, volume 202, pp. 22042–22062, 2023a.

Xingchao Liu, Chengyue Gong, and qiang liu. Flow straight and fast: Learning to generate and transfer data with rectified flow. In *The Eleventh International Conference on Learning Representations*, 2023b.

Nanye Ma, Mark Goldstein, Michael S Albergo, Nicholas M Boffi, Eric Vanden-Eijnden, and Saining Xie. Sit: Exploring flow and diffusion-based generative models with scalable interpolant transformers. *arXiv preprint arXiv:2401.08740*, 2024.

Morteza Mardani, Jiaming Song, Jan Kautz, and Arash Vahdat. A variational perspective on solving inverse problems with diffusion models. In *The Twelfth International Conference on Learning Representations*, 2024.

Xiangming Meng and Yoshiyuki Kabashima. Diffusion model based posterior sampling for noisy linear inverse problems. *arXiv preprint arXiv:2211.12343*, 2022.

Kushagra Pandey, Ruihan Yang, and Stephan Mandt. Fast samplers for inverse problems in iterative refinement models. *arXiv preprint arXiv:2405.17673*, 2024.

Ashwini Pokle, Matthew J Muckley, Ricky TQ Chen, and Brian Karrer. Training-free linear image inversion via flows. *arXiv preprint arXiv:2310.04432*, 2023.

Robin Rombach, Andreas Blattmann, Dominik Lorenz, Patrick Esser, and Björn Ommer. High-resolution image synthesis with latent diffusion models. In *Proceedings of the IEEE/CVF conference on computer vision and pattern recognition*, pp. 10684–10695, 2022.

Litu Rout, Negin Raoof, Giannis Daras, Constantine Caramanis, Alex Dimakis, and Sanjay Shakkottai. Solving linear inverse problems provably via posterior sampling with latent diffusion models. *Advances in Neural Information Processing Systems*, 36, 2024.

Chitwan Saharia, William Chan, Huiwen Chang, Chris Lee, Jonathan Ho, Tim Salimans, David Fleet, and Mohammad Norouzi. Palette: Image-to-image diffusion models. In *ACM SIGGRAPH 2022 Conference Proceedings*, SIGGRAPH '22, 2022.

Chitwan Saharia, Jonathan Ho, William Chan, Tim Salimans, David J. Fleet, and Mohammad Norouzi. Image super-resolution via iterative refinement. *IEEE Transactions on Pattern Analysis and Machine Intelligence*, 45(4):4713–4726, 2023.

Simo Särkkä and Arno Solin. *Applied stochastic differential equations*, volume 10. Cambridge University Press, 2019.

Bowen Song, Soo Min Kwon, Zecheng Zhang, Xinyu Hu, Qing Qu, and Liyue Shen. Solving inverse problems with latent diffusion models via hard data consistency. In *The Twelfth International Conference on Learning Representations*, 2024.

Jiaming Song, Chenlin Meng, and Stefano Ermon. Denoising diffusion implicit models. In *International Conference on Learning Representations*, 2021a.

Jiaming Song, Arash Vahdat, Morteza Mardani, and Jan Kautz. Pseudoinverse-guided diffusion models for inverse problems. In *International Conference on Learning Representations*, 2023.

Yang Song, Jascha Sohl-Dickstein, Diederik P Kingma, Abhishek Kumar, Stefano Ermon, and Ben Poole. Score-based generative modeling through stochastic differential equations. In *International Conference on Learning Representations*, 2021b.

Yang Song, Liyue Shen, Lei Xing, and Stefano Ermon. Solving inverse problems in medical imaging with score-based generative models. In *International Conference on Learning Representations*, 2022.

Brian L. Trippe, Luhuan Wu, Christian A. Naesseth, David Blei, and John Patrick Cunningham. Practical and asymptotically exact conditional sampling in diffusion models. In *ICML 2023 Workshop on Structured Probabilistic Inference & Generative Modeling*, 2023.

Masatoshi Uehara, Yulai Zhao, Kevin Black, Ehsan Hajiramezanali, Gabriele Scalia, Nathaniel Lee Diamant, Alex M Tseng, Tommaso Biancalani, and Sergey Levine. Fine-tuning of continuous-time diffusion models as entropy-regularized control, 2024.

Singanallur V Venkatakrishnan, Charles A Bouman, and Brendt Wohlberg. Plug-and-play priors for model based reconstruction. In *2013 IEEE global conference on signal and information processing*, pp. 945–948. IEEE, 2013.

Yinhuai Wang, Jiwen Yu, and Jian Zhang. Zero-shot image restoration using denoising diffusion null-space model. *The Eleventh International Conference on Learning Representations*, 2023.

Jay Whang, Mauricio Delbracio, Hossein Talebi, Chitwan Saharia, Alexandros G. Dimakis, and Peyman Milanfar. Deblurring via stochastic refinement. In *Proceedings of the IEEE/CVF Conference on Computer Vision and Pattern Recognition (CVPR)*, pp. 16293–16303, June 2022.

Xingyu Xu and Yuejie Chi. Provably robust score-based diffusion posterior sampling for plug-and-play image reconstruction. *arXiv preprint arXiv:2403.17042*, 2024.

Fisher Yu, Yinda Zhang, Shuran Song, Ari Seff, and Jianxiong Xiao. Lsun: Construction of a large-scale image dataset using deep learning with humans in the loop. *arXiv preprint arXiv:1506.03365*, 2015.

Benjamin Zhang, Tuhin Sahai, and Youssef Marzouk. Sampling via controlled stochastic dynamical systems. In *I (Still) Can't Believe It's Not Better! NeurIPS 2021 Workshop*, 2021.

Bingliang Zhang, Wenda Chu, Julius Berner, Chenlin Meng, Anima Anandkumar, and Yang Song. Improving diffusion inverse problem solving with decoupled noise annealing. *arXiv preprint arXiv:2407.01521*, 2024.

Richard Zhang, Phillip Isola, Alexei A Efros, Eli Shechtman, and Oliver Wang. The unreasonable effectiveness of deep features as a perceptual metric. In *Proceedings of the IEEE conference on computer vision and pattern recognition*, pp. 586–595, 2018.

Yuanzhi Zhu, Kai Zhang, Jingyun Liang, Jiezhang Cao, Bihan Wen, Radu Timofte, and Luc Van Gool. Denoising diffusion models for plug-and-play image restoration. In *2023 IEEE/CVF Conference on Computer Vision and Pattern Recognition Workshops (CVPRW)*, pp. 1219–1229, 2023.

APPENDIX: FIG: FLOW WITH INTERPOLANT GUIDANCE FOR LINEAR INVERSE PROBLEMS

A PROOFS

A.1 PROOF OF THEOREM 1

The proof follows from Appendix C of Ma et al. (2024). We start with the conditional density $\overline{p}_t(\boldsymbol{x}|\boldsymbol{y}_0, \boldsymbol{\varepsilon}_y)$ and later use Assumption 1 to get $p_t(\boldsymbol{x}|\boldsymbol{y}_t)$. Let

$$\hat{p}_t(k) = \int e^{ik\cdot\boldsymbol{x}} \overline{p}_t(\boldsymbol{x}|\boldsymbol{y}_0, \boldsymbol{\varepsilon}_y) dx \tag{23}$$

be the characteristic function, which is also equal to

$$\hat{p}_t(k) = \tilde{\mathbb{E}} e^{ik\cdot\boldsymbol{x}_t}. \tag{24}$$

Here $\tilde{\mathbb{E}}$ denote the expectation on $\boldsymbol{x}_0|\boldsymbol{y}_0, \boldsymbol{\varepsilon}_y$ and $\boldsymbol{\varepsilon}_x|\boldsymbol{y}_0, \boldsymbol{\varepsilon}_y$. Similar to Ma et al. (2024), we have

$$\begin{aligned}
\partial_t \hat{p}_t(k) &= \partial_t \tilde{\mathbb{E}} e^{ik\cdot\boldsymbol{x}_t} \\
&= ik\tilde{\mathbb{E}}(\dot{\boldsymbol{x}}_t e^{ik\cdot\boldsymbol{x}_t}) \\
&= ik\mathbb{E}_{\overline{p}_t} \tilde{\mathbb{E}}(\dot{\boldsymbol{x}}_t e^{ik\cdot\boldsymbol{x}_t}|\boldsymbol{x}_t) \\
&= ik\mathbb{E}_{\overline{p}_t}[\tilde{\mathbb{E}}(\dot{\boldsymbol{x}}_t|\boldsymbol{x}_t) e^{ik\cdot\boldsymbol{x}_t}] \\
&= ik\mathbb{E}_{\overline{p}_t}(\tilde{\boldsymbol{v}}_t(\boldsymbol{x}_t) e^{ik\cdot\boldsymbol{x}_t}),
\end{aligned} \tag{25}$$

where we define $\tilde{\boldsymbol{v}}_t(\boldsymbol{x}_t) = \tilde{\mathbb{E}}(\dot{\alpha}_t \boldsymbol{x}_0 + \dot{\sigma}_t \boldsymbol{\varepsilon}_x|\boldsymbol{x}_t) = \mathbb{E}(\dot{\alpha}_t \boldsymbol{x}_0 + \dot{\sigma}_t \boldsymbol{\varepsilon}_x|\boldsymbol{x}_t, \boldsymbol{y}_0, \boldsymbol{\varepsilon}_y)$.

Now using the two formulations of the characteristic function given in Eq. (23) and Eq. (24), we have

$$\partial_t \int e^{ik\cdot\boldsymbol{x}} \overline{p}_t(\boldsymbol{x}|\boldsymbol{y}_0, \boldsymbol{\varepsilon}_y) dx = ik \int \tilde{\boldsymbol{v}}_t(\boldsymbol{x}_t) e^{ik\cdot\boldsymbol{x}_t} \overline{p}_t(\boldsymbol{x}|\boldsymbol{y}_0, \boldsymbol{\varepsilon}_y) dx. \tag{26}$$

Thus we have

$$\begin{aligned}
&\int e^{ik\cdot\boldsymbol{x}} \partial_t \overline{p}_t(\boldsymbol{x}|\boldsymbol{y}_0, \boldsymbol{\varepsilon}_y) dx \\
=& \int \tilde{\boldsymbol{v}}_t(\boldsymbol{x}_t) \nabla_x (e^{ik\cdot\boldsymbol{x}_t}) \overline{p}_t(\boldsymbol{x}|\boldsymbol{y}_0, \boldsymbol{\varepsilon}_y) dx \\
=& -\int \nabla_x \cdot [\tilde{\boldsymbol{v}}_t(\boldsymbol{x}_t) \overline{p}_t(\boldsymbol{x}|\boldsymbol{y}_0, \boldsymbol{\varepsilon}_y)] e^{ik\cdot\boldsymbol{x}_t} dx,
\end{aligned} \tag{27}$$

where the last equality uses integration by parts. Using the inverse Fourier transform we have

$$\partial_t \overline{p}_t(\boldsymbol{x}|\boldsymbol{y}_0, \boldsymbol{\varepsilon}_y) + \nabla_x \cdot [\tilde{\boldsymbol{v}}_t(\boldsymbol{x}_t) \overline{p}_t(\boldsymbol{x}|\boldsymbol{y}_0, \boldsymbol{\varepsilon}_y)] = 0. \tag{28}$$

Since we start from $t = T$, a minus sign should be added to $\tilde{\boldsymbol{v}}$. Using Assumption 1 gives Eq. (17). Assumption 1 can also be equivalently stated as follows: let the density function of $\boldsymbol{x}_t$ given $\boldsymbol{y}_0$ and $\boldsymbol{\varepsilon}_y$ be $\overline{p}_t(\boldsymbol{x}|\boldsymbol{y}_0, \boldsymbol{\varepsilon}_y)$, then there exists p_t such that

$$\overline{p}_t(\boldsymbol{x}|\boldsymbol{y}_0, \boldsymbol{\varepsilon}_y) = p_t(\boldsymbol{x}|\boldsymbol{y}_t). \tag{29}$$

The equality holds when $\boldsymbol{\varepsilon}_y$ is independent of $\boldsymbol{\varepsilon}_x$. The proof follows the one of Equation 9 by Ma et al. (2024).

$$\begin{aligned}
\boldsymbol{v}_t(\boldsymbol{x}|\boldsymbol{y}_t) &= \dot{\alpha}_t \mathbb{E}[\boldsymbol{x}_*|\boldsymbol{x}, \boldsymbol{y}_t] + \dot{\sigma}_t \mathbb{E}[\boldsymbol{\varepsilon}_x|\boldsymbol{x}, \boldsymbol{y}_t] \\
&= \dot{\alpha}_t \mathbb{E}\left[\frac{\boldsymbol{x}_t - \sigma_t \boldsymbol{\varepsilon}}{\alpha_t} \middle| \boldsymbol{x}, \boldsymbol{y}_t\right] + \dot{\sigma}_t \mathbb{E}[\boldsymbol{\varepsilon}_x|\boldsymbol{x}, \boldsymbol{y}_t] \\
&= \frac{\dot{\alpha}_t}{\alpha_t}\boldsymbol{x} + \left(\dot{\sigma}_t - \frac{\dot{\alpha}_t \sigma_t}{\alpha_t}\right) \mathbb{E}[\boldsymbol{\varepsilon}_x|\boldsymbol{x}, \boldsymbol{y}_t] \\
&= \frac{\dot{\alpha}_t}{\alpha_t}\boldsymbol{x} + \left(\dot{\sigma}_t - \frac{\dot{\alpha}_t \sigma_t}{\alpha_t}\right) (-\sigma_t \boldsymbol{s}_t(\boldsymbol{x}|\boldsymbol{y}_t)) \\
&= \frac{\dot{\alpha}_t}{\alpha_t}\boldsymbol{x} - \lambda_t \sigma_t \boldsymbol{s}_t(\boldsymbol{x}|\boldsymbol{y}_t)
\end{aligned} \tag{30}$$

Algorithm 2 FIG+

Require: T, c, K, w, m, $\boldsymbol{y}_0$

Initialize $\boldsymbol{x}_T = \boldsymbol{\varepsilon}_x \sim \mathcal{N}(\mathbf{0}, \boldsymbol{I})$ ▷ Initialize $\boldsymbol{x}_t$
$\Delta t = 1/T$
for $i = T$ **to** 1 **do**
  $t = i/T, t' = (i-1)/T$
  $\boldsymbol{y}_{i-1} = \alpha_{t'}\boldsymbol{y}_0 + w\sigma_{t'}\boldsymbol{A}\boldsymbol{\varepsilon}_x$ ▷ measurement interpolation with rescaled variance
  $\boldsymbol{x}_{i-1} = \boldsymbol{x}_i - \boldsymbol{v}_\theta(\boldsymbol{x}_i, t)\Delta t$ ▷ Unconditional update
  for $k = 1$ **to** K **do**
    $\boldsymbol{x}_{i-1} = \boldsymbol{x}_{i-1} - \frac{c\lambda_t\sigma_t\Delta t}{2\alpha_t^2\sigma_n^2}\nabla_{\boldsymbol{x}_{i-1}}\|\boldsymbol{y}_{i-1} - \boldsymbol{A}\boldsymbol{x}_{i-1}\|_2^2$ ▷ K-times conditional update
  end for
  $\boldsymbol{x}'_0 = (1-t)\boldsymbol{v}_\theta(\boldsymbol{x}_i, t) + \boldsymbol{x}_i$ ▷ use Tweedie's formula to estimate $\boldsymbol{x}_0$
  $\boldsymbol{x}'_{i-1} = \alpha_{i-1}\boldsymbol{x}'_0 + \sigma_{i-1}\boldsymbol{\varepsilon}_x$ ▷ perturb estimated $\boldsymbol{x}_0$ to time t_{i-1}
  $\boldsymbol{x}_{i-1} = \boldsymbol{A}\boldsymbol{x}_{i-1} + (1-m)(\boldsymbol{I} - \boldsymbol{A})\boldsymbol{x}_{i-1} + m(\boldsymbol{I} - \boldsymbol{A})\boldsymbol{x}'_{i-1}$ ▷ mix $\boldsymbol{x}'_{i-1}$ with $\boldsymbol{x}_{i-1}$
end for

A.2 Proof of Corollary 1

From Eq. (16), the first update for $\boldsymbol{x}'_{i-1}$ uses information of $\boldsymbol{x}_i$. If we now consider the second step first and then it's next update step, the update scheme reads as follows:

$$\begin{cases} \boldsymbol{x}_{i-1} &= \boldsymbol{x}'_{i-1} - \frac{\lambda_t\sigma_t}{2\alpha_t^2\sigma_n^2}\nabla_{x'_{i-1}}\|\boldsymbol{y}_{i-1} - \boldsymbol{A}\boldsymbol{x}'_{i-1}\|^2\Delta t \\ \boldsymbol{x}'_{i-2} &= \boldsymbol{x}_{i-1} - \boldsymbol{v}_{t_{i-1}}(\boldsymbol{x}_{i-1})\Delta t, \end{cases} \tag{31}$$

which is a splitting of

$$-\Big(\frac{\dot{\alpha}_{t_{i-1}}}{\alpha_{t_{i-1}}}\boldsymbol{x} - \lambda_{t_{i-1}}\sigma_{t_{i-1}}\nabla_x \log p_{t_{i-1}}(\boldsymbol{x}|\boldsymbol{y}_{t_{i-1}})\Big)dt. \tag{32}$$

This completes the proof.

A.3 Proof of Corollary 2

The corollary is a direct result of Theorem 1. The velocity field of diffusion models is defined in the probability flow ODE (Song et al., 2021b), which is exactly Eq. (22) when conditioning on $\boldsymbol{y}_t$.

B FIG+ Algorithm

We provide the FIG+ algorithm in Algorithm 2.

C Ablation Study

C.1 K-Times Conditional Update

In this section, we perform the ablation study over the K-times conditional update strategy.

(a) Reference (b) Measure (c) $K = 1$ (d) Overfit (e) optimal K

Figure 7: Our FIG algorithm for Gaussian deblurring and random inpainting with noise $\sigma_n = 0.05$ on the CelebA-HQ dataset.

	SR (4×)			**Gaussian Deblur**			**Colorization**			**Inpainting**		
Method	PSNR ↑	SSIM ↑	LPIPS ↓	PSNR ↑	SSIM ↑	LPIPS ↓	PSNR ↑	SSIM ↑	LPIPS ↓	PSNR ↑	SSIM ↑	LPIPS ↓
$K = 1$	28.51	0.812	0.222	25.43	0.691	0.271	24.21	0.902	0.241	30.02	0.895	0.189
optimal K	28.51	0.812	0.222	26.45	0.738	0.257	24.21	0.902	0.241	33.33	0.920	0.131

Table 4: Quantitative comparison (PSNR, SSIM, LPIPS) of our algorithm for different K's on the CelebA-HQ 256×256 validation set. All input images have a measurement Gaussian noise of $\sigma_n = 0.05$. Note that for SR (4×) and colorization, the optimal $K = 1$, so they have the same metrics.

	SR (4×)			**Gaussian Deblur**			**Colorization**			**Inpainting**		
Method	PSNR ↑	SSIM ↑	LPIPS ↓	PSNR ↑	SSIM ↑	LPIPS ↓	PSNR ↑	SSIM ↑	LPIPS ↓	PSNR ↑	SSIM ↑	LPIPS ↓
$K = 1$	24.48	0.646	0.370	22.75	0.533	0.445	24.27	0.862	0.284	27.25	0.815	0.246
optimal K	24.48	0.646	0.370	23.36	0.554	0.433	24.27	0.862	0.284	29.17	0.872	0.156

Table 5: Quantitative comparison (PSNR, SSIM, LPIPS) of our algorithm for different K's on the LSUN-Bedroom 256×256 validation set. All input images have a measurement Gaussian noise of $\sigma_n = 0.05$. Note that for SR (4×) and colorization, the optimal $K = 1$, so they have the same metrics.

	SR (4×)			**Gaussian Deblur**			**Colorization**			**Inpainting**		
Method	PSNR ↑	SSIM ↑	LPIPS ↓	PSNR ↑	SSIM ↑	LPIPS ↓	PSNR ↑	SSIM ↑	LPIPS ↓	PSNR ↑	SSIM ↑	LPIPS ↓
$K = 1$	28.45	0.730	0.260	25.33	0.590	0.330	25.52	0.906	0.246	31.04	0.867	0.178
optimal K	28.45	0.730	0.260	26.25	0.632	0.310	25.52	0.906	0.246	31.04	0.867	0.178

Table 6: Quantitative comparison (PSNR, SSIM, LPIPS) of our algorithm for different K's on the AFHQ-Cat 256×256 validation set. All input images have a measurement Gaussian noise of $\sigma_n = 0.05$. Note that for SR (4×), colorization, and inpainting, the optimal $K = 1$, so they have the same metrics.

We run experiments with $K = 1$ and the optimal K. For both experiments, we finetune other hyperparameters so that our algorithm achieves the best performance under certain K settings. Fig. 7

contains examples of Gaussian deblurring and random inpainting on the CelebA-HQ dataset. When we set $K = 1$, the results are blurry and exhibit unnatural details compared to the result for the optimal K. If we fully minimize the distance $\|\boldsymbol{y}_t - \boldsymbol{A}\boldsymbol{x}_t\|_2^2$ at each timestep, the output shows severe overfitting problems as illustrated in Fig. 7d. To mitigate the risk, we tune K and c for better performance. The quantitative results are shown in Table 4, Table 5, and Table 6.

C.2 Measurement Interpolant Variance Rescaling

In this section, we ablate the measurement interpolant variance rescaling technique.

(a) Reference (b) Measure (c) $w = 1$ (d) optimal w

Figure 8: Our FIG algorithm for super-resolution and random inpainting with noise $\sigma_n = 0.05$ on the LSUN-Bedroom and AFHQ-Cat datasets.

	SR (4×)			**Gaussian Deblur**			**Colorization**			**Inpainting**		
Method	PSNR ↑	SSIM ↑	LPIPS ↓	PSNR ↑	SSIM ↑	LPIPS ↓	PSNR ↑	SSIM ↑	LPIPS ↓	PSNR ↑	SSIM ↑	LPIPS ↓
$w = 1$	25.66	0.585	0.376	24.08	0.533	0.383	23.24	0.673	0.400	19.36	0.407	0.495
optimal w	28.51	0.812	0.222	26.45	0.738	0.257	24.21	0.902	0.241	33.33	0.920	0.131

Table 7: Quantitative comparison (PSNR, SSIM, LPIPS) of our algorithm for different w's on the CelebA-HQ 256×256 validation set. All input images have a measurement Gaussian noise of $\sigma_n = 0.05$.

	SR (4×)			**Gaussian Deblur**			**Colorization**			**Inpainting**		
Method	PSNR ↑	SSIM ↑	LPIPS ↓	PSNR ↑	SSIM ↑	LPIPS ↓	PSNR ↑	SSIM ↑	LPIPS ↓	PSNR ↑	SSIM ↑	LPIPS ↓
$w = 1$	21.02	0.327	0.566	20.06	0.273	0.575	19.80	0.486	0.557	19.48	0.346	0.571
optimal w	24.48	0.646	0.370	23.36	0.554	0.433	24.27	0.862	0.284	29.17	0.872	0.156

Table 8: Quantitative comparison (PSNR, SSIM, LPIPS) of our algorithm for different w's on the LSUN-Bedroom 256×256 validation set. All input images have a measurement Gaussian noise of $\sigma_n = 0.05$.

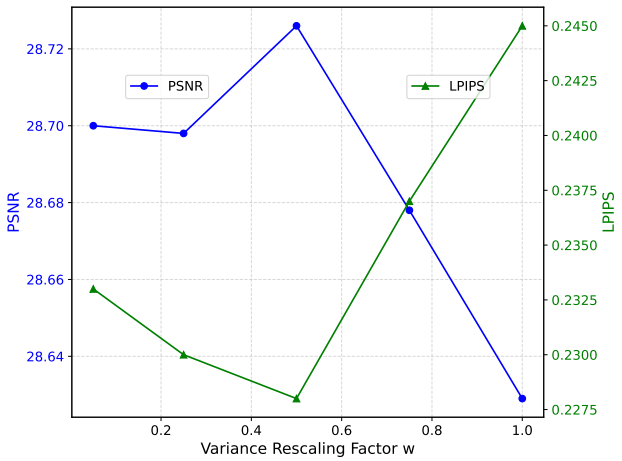

Figure 9: Metrics for $4\times$ super resolution on CelebA-HQ 256×256 validation set with different variance rescaling factor w.

	SR ($4\times$)			**Gaussian Deblur**			**Colorization**			**Inpainting**		
Method	PSNR ↑	SSIM ↑	LPIPS ↓	PSNR ↑	SSIM ↑	LPIPS ↓	PSNR ↑	SSIM ↑	LPIPS ↓	PSNR ↑	SSIM ↑	LPIPS ↓
$w = 1$	26.02	0.538	0.395	24.74	0.466	0.419	23.95	0.685	0.441	21.76	0.388	0.523
optimal w	28.45	0.730	0.260	26.25	0.632	0.310	25.52	0.906	0.246	31.04	0.867	0.178

Table 9: Quantitative comparison (PSNR, SSIM, LPIPS) of our algorithm for different w's on the AFHQ-Cat 256×256 validation set. All input images have a measurement Gaussian noise of $\sigma_n = 0.05$.

In our algorithm, the measurement interpolant is defined as $\boldsymbol{y}_t = \alpha_t \boldsymbol{y}_0 + w\sigma_t \boldsymbol{\varepsilon}_y$. Without rescaling, i.e., for $w = 1$, as shown in the first row in Fig. 8, we observe that the reconstructed result appears as if two images have been combined: one representing our measurement and the other determined by the initialization and the ODE. Increasing the weight of the measurement guidance can address this issue, but it leads to overfitting, resulting in a high level of noise in the final output as shown in the second row in Fig. 8. With a smaller optimal w, we can achieve a balance between these two situations, resulting in much better outcomes. The quantitative results are presented in Tables 7 to 9. All experiments are conducted with optimal hyperparameters. Fig. 9 gives a visual illustration of effects on different w for super resolution on CelebA with flow matching prior. It's clear that w affects the performance of our algorithm and there exists an optimal w. We only show the PSNR and LPIPS because the SSIM scores are close.

D Recovery vs Perceptual Trade-off

Method	PSNR ↑	SSIM ↑	LPIPS ↓	FID ↓	KID ↓
FIG-Diffusion	**29.89**	**0.846**	0.163	25.46	0.013
DPS-Diffusion	28.85	0.801	0.172	**19.31**	**0.005**
DDNM+	28.82	0.750	0.340	64.85	0.052
DAPS	29.59	0.809	0.158	23.69	0.013
C-ΠGDM	28.14	0.787	**0.106**	30.51	0.019

Table 10: Quantitative comparison (PSNR, SSIM, LPIPS, FID, KID) of different algorithms for $4\times$ super-resolution with noise $\sigma_n = 0.05$ on the CelebA-HQ 256×256 test dataset. **Bold** for the best.

(a) Reference (b) Average pooling (c) Bicubic

Figure 10: DDNM+ results for $4\times$ bicubic super-resolution with noise $\sigma_n = 0.05$ on the CelebA-HQ dataset.

In this section, we report FID and KID along with the metrics used in the main paper, i.e., PSNR, SSIM, and LPIPS for $4\times$ super-resolution with noise $\sigma_n = 0.05$ on the CelebA-HQ 256×256 (see Table 10), and discuss the recovery and perceptual trade-off in those metrics.

PSNR and SSIM are considered recovery metrics that measure pixel-level fidelity while LPIPS, FID, and KID are referred to as perceptual metrics that assess perceptual similarity or high-level semantic fidelity.

In this paper, we focus on image reconstruction tasks involving noisy measurements. In this case, metrics like FID and KID, while effective for generative models emphasizing perceptual realism, evaluate distribution-level similarity and may fail to capture details in structural recovery, particularly in high-noise scenarios where subtle details matter. Additionally, FID and KID can be misleading if the reconstructed images are perceptually plausible but deviate significantly from the ground truth. PSNR and SSIM, however, provide a clear and objective measure of how well the noise has been suppressed and the original content preserved, which remains critical in our experiments.

As shown in Table 10, our algorithm achieves a balanced trade-off between recovery and perceptual metrics. In the task of noisy image reconstruction, it not only delivers the best recovery metrics but also achieves impressive perceptual scores.

E Baseline Implementations

For the pretrained model, we use both flow matching and diffusion models. For all algorithms with a flow matching base model, we use the rectified flow.[1] For measurement operators, since our baseline methods OT-ODE and DMPS require an SVD, we inherit codes from the DDRM Github repository.

DPS-Flow. In the codes for the Rectified flow model, $\alpha_t = t$ and $\sigma_t = 1 - t$. Following Eq. (18), we have $\hat{\boldsymbol{x}}_0 = (1-t)\boldsymbol{v}_\theta(\boldsymbol{x}_t, t) + \boldsymbol{x}_t$. Given $\hat{\boldsymbol{x}}_0$, we implement DPS strictly following Algorithm 1 of (Chung et al., 2023b) and fine-tune the hyperparameter ζ_i to achieve the best performance.

DMPS. With the SVD operations from DDRM codes, we implement DMPS strictly following Algorithm 1 in (Meng & Kabashima, 2022) and fine-tune the hyperparameter λ to get the best results. Again, the score function is obtained by the velocity following Eq. (18).

OT-ODE. Using the same $\hat{\boldsymbol{x}}_0$ as DPS and the SVD operations from the DDRM implementation, we implement the OT-ODE strictly following Algorithm 1 of (Pokle et al., 2023) and test the start time for each task to get the best performance.

DAPS. We use the official repository[2] and strictly follow the Algorithm 1 of Zhang et al. (2024) to implement DAPS.

DPS-Diffusion. We implement DPS on the EDM implementation from the DAPS repository.

[1] https://github.com/gnobitab/RectifiedFlow

[2] https://github.com/zhangbingliang2019/DAPS

Method	SR (4×)			Gaussian Deblur			Colorization			Inpainting		
	PSNR ↑	SSIM ↑	LPIPS ↓	PSNR ↑	SSIM ↑	LPIPS ↓	PSNR ↑	SSIM ↑	LPIPS ↓	PSNR ↑	SSIM ↑	LPIPS ↓
FIG (ours)	**24.54**	**0.682**	**0.327**	**22.94**	**0.588**	0.402	21.87	**0.865**	**0.320**	**30.24**	**0.895**	**0.139**
DPS	24.23	0.649	0.346	19.82	0.433	0.471	14.30	0.610	0.596	27.21	0.771	0.283
DMPS	24.08	0.653	0.368	22.76	0.575	0.413	21.26	**0.865**	0.326	27.34	0.841	0.212
OT-ODE	23.82	0.639	0.349	22.16	0.566	**0.389**	**22.06**	0.781	0.385	26.56	0.768	0.278

Table 11: Quantitative comparison (PSNR, SSIM, LPIPS) of different algorithms for different tasks on the LSUN-Bedroom 256×256 test dataset. All input images have a measurement Gaussian noise of $\sigma_n = 0.05$. **Bold** for the best.

Method	SR (4×)			Gaussian Deblur			Colorization			Inpainting		
	PSNR ↑	SSIM ↑	LPIPS ↓	PSNR ↑	SSIM ↑	LPIPS ↓	PSNR ↑	SSIM ↑	LPIPS ↓	PSNR ↑	SSIM ↑	LPIPS ↓
FIG (ours)	**27.50**	0.707	**0.272**	**25.14**	**0.591**	**0.334**	**26.36**	**0.915**	0.227	**28.99**	**0.835**	**0.202**
DPS	25.70	0.607	0.332	21.40	0.407	0.429	21.82	0.763	0.407	26.20	0.709	0.300
DMPS	27.49	**0.709**	0.286	24.97	0.577	0.343	26.12	0.913	**0.221**	27.02	0.781	0.262
OT-ODE	25.95	0.617	0.326	24.42	0.536	0.357	25.39	0.849	0.291	28.22	0.789	0.235

Table 12: Quantitative comparison (PSNR, SSIM, LPIPS) of different algorithms for different tasks on the AFHQ-Cat 256×256 test dataset. All input images have a measurement Gaussian noise of $\sigma_n = 0.05$. **Bold** for the best.

DDNM/DDNM+. We implement DDNM and DDNM+ strictly following Algorithm 1 and 2 of Wang et al. (2023).[3] We reproduce all the metrics of the tasks reported in their paper but find that the performance of DDNM/DDNM+ varies significantly across different tasks. Our experiment shows that DDNM/DDNM+ fails on Gaussian deblurring with noise, which matches the result of Meng & Kabashima (2022). We also find that DDNM/DDNM+ can't handle super-resolution with bicubic down-sampling well, resulting in noisy reconstructions as shown in Fig. 10. However for super-resolution with average pooling, we achieved good results for both SR($4\times$) with noise standard deviation 0.05 and SR($16\times$) with noise standard deviation 0.2. Motion deblur is not implemented since DDNM requires SVD operations.

C-ΠGDM. We implement C-ΠGDM strictly following Algorithm 1 of Pandey et al. (2024).[4] We reproduce all the metrics of the tasks reported in their paper and find that the performance varies significantly across different measurement noise levels. Our experiment shows that C-ΠGDM fails on Gaussian deblurring and 90% random inpainting with noise. However, we find C-ΠGDM results are especially competitive in terms of LPIPS, and the runtime is much lower than all other baseline methods we include. Motion deblur is not implemented since SVD operations are required.

F Additional Experimental Results for Flow Matching Model

We show additional results with flow matching priors. Reconstructed images for motion deblurring with $\sigma_n = 0.05$ on CelebA-HQ are shown in Fig. 11. Additional quantitative results on other datasets (LSUN-Bedroom, AFHQ-Cat) are shown in Tables 11 and 12.

[3] https://github.com/wyhuai/DDNM

[4] https://github.com/mandt-lab/c-pigdm

(a) Reference (b) Measure (c) DPS (d) DMPS (e) OT-ODE (f) FIG (ours)

Figure 11: Results for motion deblurring with noise $\sigma_n = 0.05$ on the CelebA-HQ dataset.

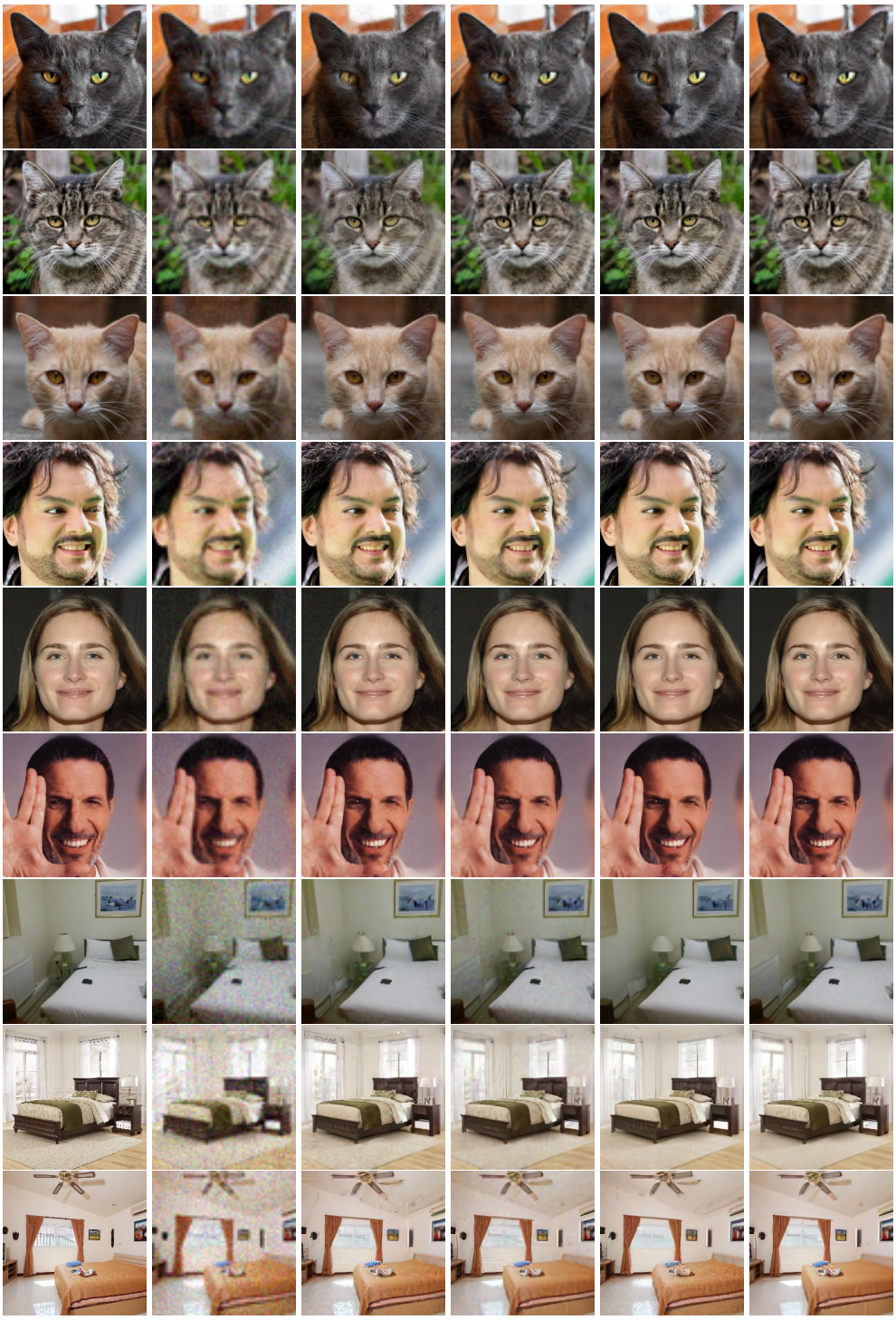

(a) Reference (b) Measure (c) DPS (d) DMPS (e) OT-ODE (f) FIG (ours)

Figure 12: Results for super-resolution ($4\times$) with noise $\sigma_n = 0.05$ on AFHQ-Cat, CelebA-HQ, and LSUN-Bedroom datasets.

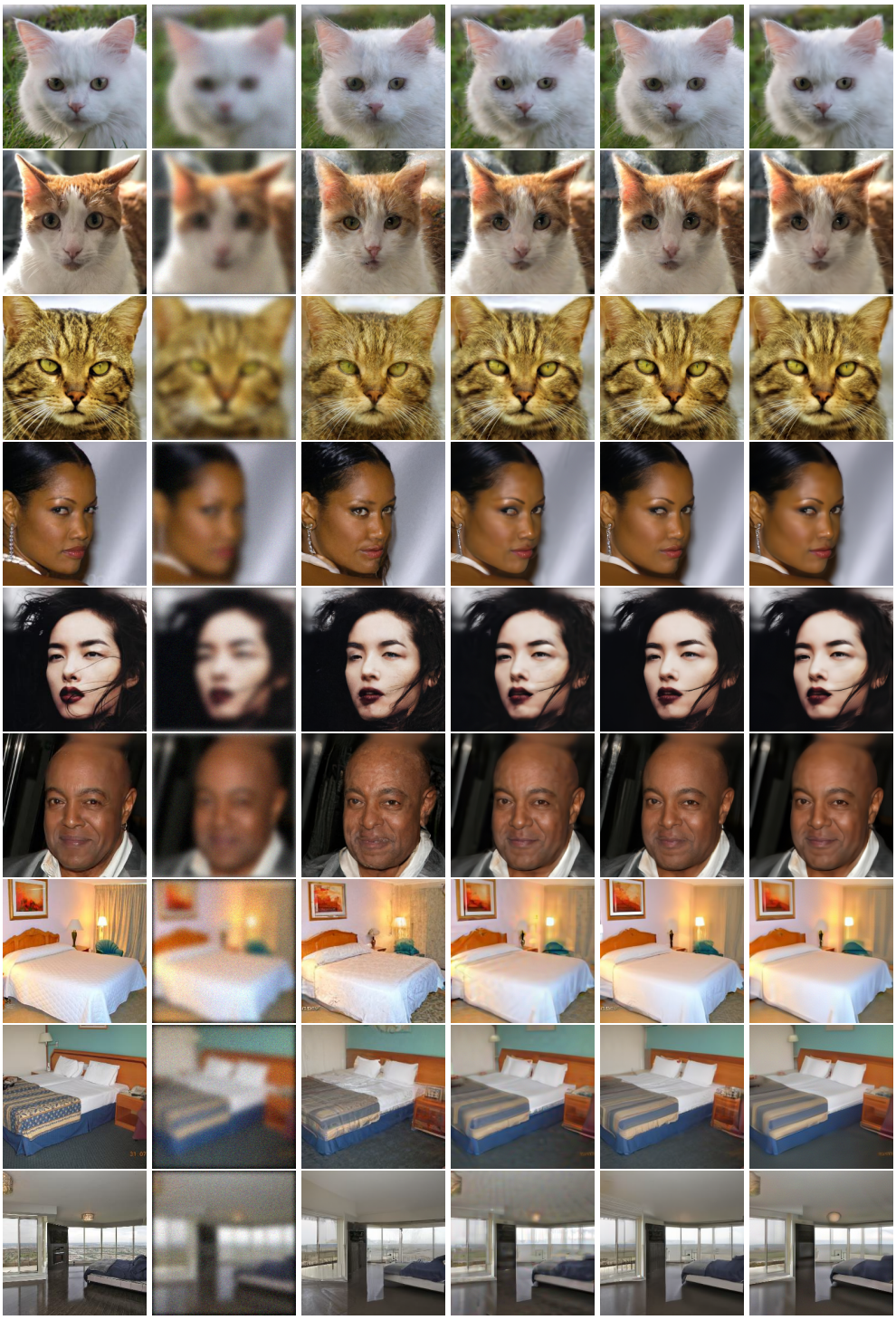

(a) Reference (b) Measure (c) DPS (d) DMPS (e) OT-ODE (f) FIG (ours)

Figure 13: Results for Gaussian deblurring with noise $\sigma_n = 0.05$ on AFHQ-Cat, CelebA-HQ, and LSUN-Bedroom datasets.

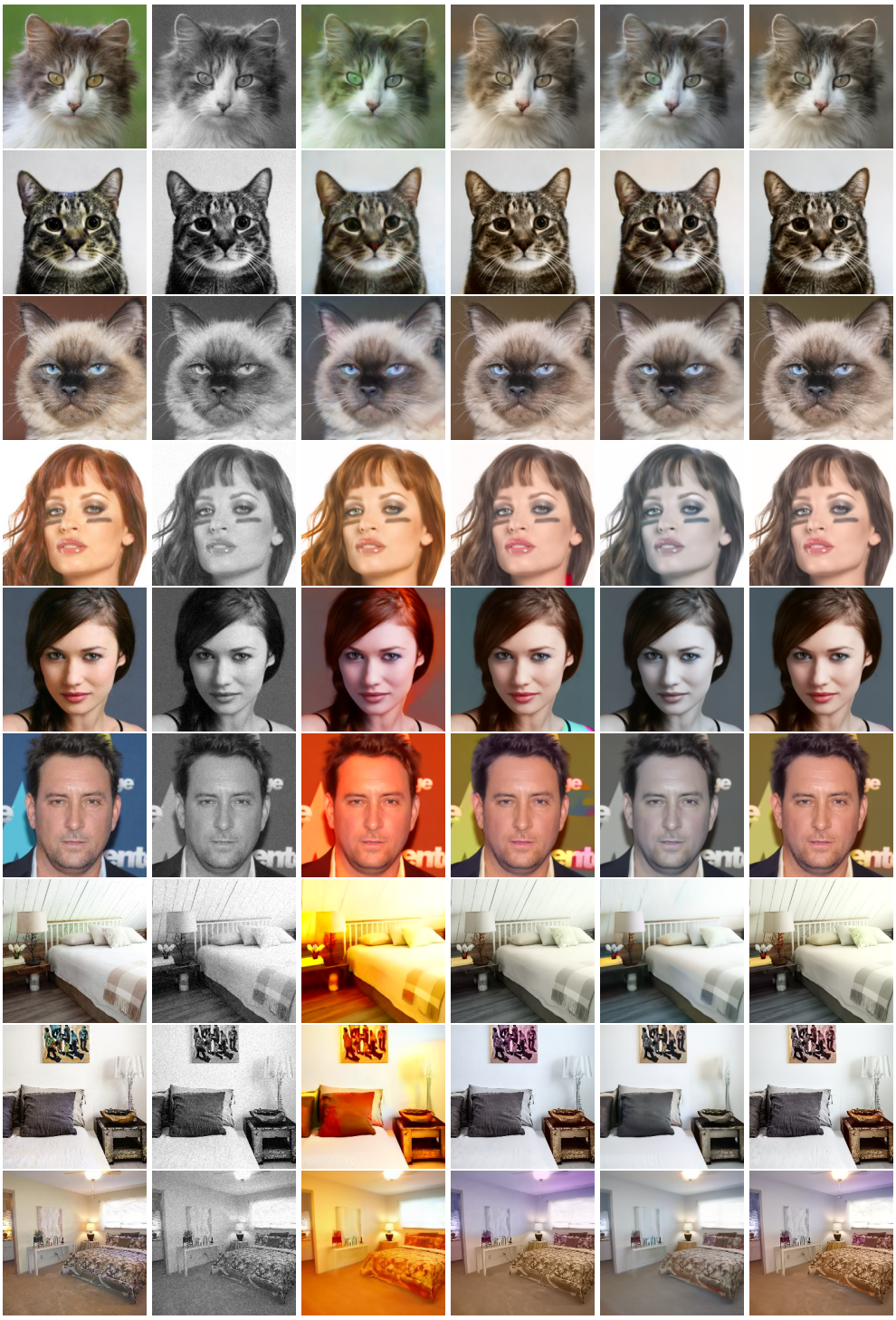

(a) Reference (b) Measure (c) DPS (d) DMPS (e) OT-ODE (f) FIG (ours)

Figure 14: Results for colorization with noise $\sigma_n = 0.05$ on AFHQ-Cat, CelebA-HQ, and LSUN-Bedroom datasets.

G ADDITIONAL EXPERIMENT RESULTS FOR DIFFUSION MODEL

In this section, we show that our algorithm works for diffusion models. Qualitative results are shown below.

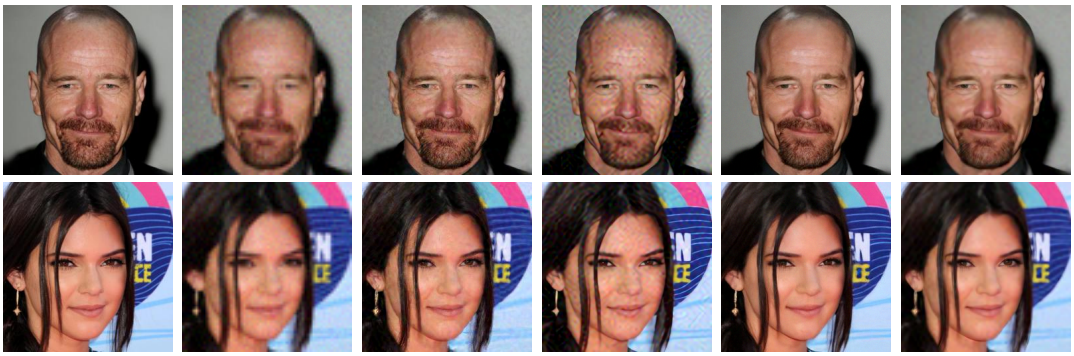

(a) Reference (b) Measure (c) DPS (d) DDNM+ (e) DAPS (f) FIG (ours)

Figure 15: Results for $4\times$ bicubic super-resolution with noise $\sigma_n = 0.05$ on the CelebA-HQ dataset.

(a) Reference (b) Measure (c) DPS (d) DDNM+ (e) DAPS (f) FIG (ours)

Figure 16: Results for Gaussian deblurring with noise $\sigma_n = 0.05$ on the CelebA-HQ dataset.

(a) Reference (b) Measure (c) DPS (d) DAPS (e) FIG (ours)

Figure 17: Results for motion deblurring with noise $\sigma_n = 0.05$ on CelebA-HQ dataset.